Experimental Constraints on MCP Avalanche Simulations Using a Pulsed, sub-Picosecond Laser

Matthew J Wetstein[a,b], Bernhard Adams[a], Matthieu Chollet[a], Preston Webster[c,1], Zeke Insepov[a], Valentin Ivanov, Slade Jokela[a], Igor Veryovkin[a], Alex Zinovev[a], Jeffrey Elam[a], Anil Mane[a], Qing Peng[a,2], Razib Obaid[b], Alexander Vostrikov[b], Andrey Elagin[b], Henry Frisch[a,b], on behalf of the LAPPD collaboration

[a] *Argonne National Laboratory*
[b] *Enrico Fermi Institute, University of Chicago*
[c] *Iowa State University*

Abstract

Gain and timing characteristics of microchannel plates (MCPs) are determined both by the kinematics of electrons accelerating in and striking the MCP pore, and by the material propeties of the pore surface. Of particular importance are the Secondary Electron Yield (SEY), which describes the number of additional electrons produced when an electron strikes a surface material, and the forward-scattering (FS) probability, which describes the probability of an incident primary undergoing quasi-eleastic, specular reflection and keeping most of its kinetic energy. Both of these properties depend on the energies and striking angles of the incident electrons. Comparisons between simulations and experimental measurements can be used to help understand the relationship between the material properties of an MCP and the resulting cascade and, in particular, how changes in operational voltage should affect the resulting characteristics of the cascade. With the development of atomic layer deposition (ALD) techniques for fabricating MCPs there is now an opportunity to widely vary the composition of the material on the pore surface. This allows us to study MCP functionality over a much larger range of parameters than are available to conventional microchannel plates. In this paper we present a comparison between experimental measurements of ALD-functionalized MCPs with the results of a full, particle-tracking MCP Monte Carlo (MC), taking measured, material-level electron scattering properties as its inputs. Tests were performed on two MCP samples with different ALD coatings, 20 nm Al_2O_3 and 20 nm of MgO. Material level measurements were performed on silicon wafers coated with the same ALD layers and used as inputs to the full MCP simulation. This full simulation is used to predict how differences between the two materials translate to different gain-voltage dependecies. It also clarifies the internal processes driving these dependences. Methods like the one desribed in this paper can be used to further clarify the relationship between surface physics and avalanche formation, and also used in the optimization of highly customizable MCP photodetectors

Keywords: microchannel, MCP, characterization, photodetectors, time-of-flight, time-resolving
PACS: 12.38.Qk, 13.85.Qk, 14.70.Hp, 12.38.Lg

Email address: mwetstein@anl.gov (Matthew J Wetstein)
[1] Present address is Arizona State University.
[2] Present address is Duke University.

Contents

List of Figures

1. Introduction

We present a complete experimental data-Monte Carlo cycle, where simulated MCP avalanches based on material-level characterization of the surface materials are compared with device-level experimental data from MCPs made of those materials. These complete, particle-tracking simulations of MCP avalanches can be used to fundamentally understand and optimize design of microchannel plates. Similarly, experimental measurements of the timing and gain characteristics of MCPs, especially their dependences on various operational parameters, can serve to help constrain these simulations and help to understand which material-level properties have the largest impact on macroscopic device performance.

Central to our project is the use of Atomic Layer Deposition (ALD) to mass produce MCPs from low cost substrates. ALD is a batch process whereby materials can be applied uniformly and conformally to large surface areas in bulk, one molecular mono-layer at a time [1, 2]. The structure of LAPPD-made MCPs is provided by inactive, porous glass discs, cut from hexagonally-packed bundles of drawn capillaries with 20 or 40 micron pore structures and corresponding 25 or 50 micron center-to-center spacing. The substrates are ALD coated, first with a layer of resistive material and then with a high SEE layer. This presents our effort with a unique opportunity for MCP optimization [3]. Independent control over the geometric, resistive, and SEE characteristics of MCPs enables the production of channel plates with combinations of properties not easily achievable through traditional fabrication methods. By developing and testing MCPs with a wider range of possible properties, we can place stronger constraints on models of MCP behavior.

The performance of a complete MCP detector depends not only on the channel plates themselves, but also their combinations, along with a photocathode, a particular choice of anode structure, and electronic readout. In the LAPPD design, charge from the MCPs is received by a microstripline anode structure, optimized for high-bandwidth electronics. This delay-line design greatly reduces the necessary channel count, as electronic resources scale only with the square root of the area. Hit positions are determined by the signal centroid in the direction perpendicular to the striplines, and by the difference in the arrival time at the two ends of the striplines, in the direction parallel to the strips. Arrival times and gains of the pulse trains are measured by waveform sampling, which offers the best timing resolution. At the ANL-APS Laboratory, we study not only the performance of the microchannel plates, but also the issues related to systems integration of these MCPs with photocathodes and various anode designs.

2. Experimental Measurements

2.1. Sample Preparation and Material-Level Characterization

Systematic comparison of gain and timing for MCPs with identical resistance, but two different SEY layers. We used two 33mm diameter, 1.2mm thick borosilicate substrates with 20 micron pores. Both plates were treated with the resistive coating at the same time, yielding matched resistances and a common resistive chemistry. After the resistive coating, each plate was coated with a unique SEY layer: 20 nm Al_2O_3, and 20 nm MgO. In order to test the SEY properties of the resistive layer itself, both plates were masked so that the SEY chemistry was applied to only half of the MCP. However, testing later showed no signal in the resistive layer-only region. In addition to two MCPs, two 1mm x 1mm square silicon substrates were coated with the SEY layers, in order to test the SEY yield directly. The SEY curves derrived from these test coupons were later used as inputs in our simulations.

2.2. SEY Characteriztion of MCP Coatings

Secondary electron emission measurements were made using a custom-built surface characterization apparatus that included an X-ray Photoelectron Spectrometer (XPS) with hemispherical energy analyzer, Low Energy Electron Diffraction (LEED) module, and Ar-ion source for surface cleaning and milling. The LEED module was modified so that it could serve as a pulsed electron source in order to mitigate sample charging. The screen and retarding grids of the LEED module were electrically connected in order to serve as a collector for secondary electrons being emitted from the sample. During these measurements it was noticed that emission strongly depended on sample bias when in the range of 0 to -150 V. For a bias more negative than -150 V, the change in secondary electron yield became negligible with respect to change in sample bias. Therefore, a sample bias of -200 V was chosen. With this bias and the limitation of 1 keV from the LEED electron gun, we were able to measure the secondary electron yield using primary electrons with kinetic energies between 5 and 800 eV.

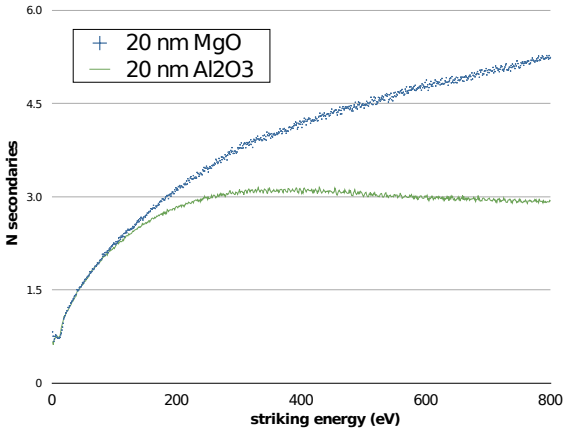

Figure 1: Measured secondary electron yield curves for electrons at normal incidence on MgO and Al_2O_3.

Conductive-silicon substrates were placed in the ALD reactor with the MCPs during the SEY layer deposition. These Si substrates serve as test coupons for the SEY layer alone. The resulting samples consisted of 3 conductive-Si substrates coated with 2 nm MgO, 20 nm MgO, and 20 nm Al2O3. These sample thicknesses were chosen to represent the extreme cases, onset of useful emission on one end and onset of sample charging on the other, as determine from past experiments [4].

The results indicate that as a secondary electron emitter, MgO is superior to Al2O3, especially for higher kinetic energy primary electrons. For low energy, the SEY is expected to approach zero. This discrepancy in the data can be explained by the defocusing of the primary electron beam and its partial deflection into the detector. When examining the 2 nm MgO film, it is observed that the emission decreases for higher kinetic energy primary electrons. This is due to the electrons penetrating through the SEY film and into the Si suFStrate, which has a much lower secondary electron yield.

2.3. Testing of Microchannel Plates

2.3.1. Experimental Setup

Tests were performed in a custom built vacuum chamber, capable of operating at vacua of order 10^{-7} and designed to accomodate our MCP test assemly opposite a fused silica window for transmitting UV to the channel plates.

The MCP samples were mounted in a flange system designed to accommodate combinations of one, two, or three MCPs with a simple aluminum thin film photocathode (chosen for its robustness in air) and a delay-line anode structure. The 33 mm samples were assembled into a special, compact holder designed at Berkeley SSL, where the spacings between the different components could be varied by swapping interchangeable, insulating spacers of different thicknesses. The voltages at each point in the MCP stacks were independently controllable. High frequency RF cables were used to bring the signal to a multi-GHz bandwidth oscilloscope.

We used a Ti:Sapphire laser to generate intense pulses of infrared light, shorter than 100 femtoseconds at a repetition rate of 1 kHz. The laser light was sent through two frequency-doubling beta-barium borate (BBO) crystals to produce UV wavelengths at around 266 nm with a beam spot size of half a millimeter on the photocathode. The oscilloscope trigger signal was derived from laser light incident on a fast photodiode with time jitter well below a picosecond.

2.3.2. Data Collection Procedure and Experimental Scans

The setup described in Section 2.3.1 allowed us to perform accurate gain and timing measurements on the entire detection system. It also allowed us to explore parameter dependencies of individual components.

Using the laser pulses as an external trigger, we coulc establish the arrival time of the light pulses with accuracies better than a picosecond. This permitted accurate measurement of the jitter in arrival times, the so-called “transit time

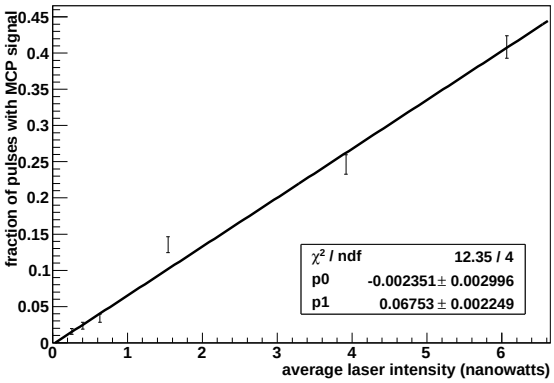

Figure 2: Laser intensity versus the fraction of laser pulses yielding an MCP signal. Data points are fit with a straight line of slope p_1 and offset p_0.

spread" (TTS), even though absolute delays due to optical paths and cabling are currently only known within tens of picoseconds. Use of a pulsed laser also greatly facilitated gain measurements: by simply attenuating to the point where only a fraction f of the pulses yield a signal, we could operate in the single photoelectron regime, with the fraction f^2 being the probability of two-photoelectron events. This eliminated the need for detailed calibration of the photocathode quantum yield. Figure 2 shows the relationship between average UV intensity and the probability of a signal from a particular photocathode combined with two commercial MCPs operating in saturation mode. This high-gain MCP configuration is necessary in order to assure that the detection probability of the stack is dominated by the yield of the photocathode and not by the channel plates. Once derived, the slope in Fig 2 could be used to extrapolate to higher intensities and allow for good control over the average number of photoelectrons. In this paper, we used higher light intensities, far about the single PE threshold, in order to see strong single plate signal.

A full series of pulsed tests were performed on our ensemble of two MCPs, made with identical resistances, but different SEE layers. We tested them as single plates, without a second MCP amplification stage. Since the signals from the lone MCPs were small, the laser intensity was set high enough to produce an average of roughly 5 photoelectrons per pulse. The readout was passed through 18 GHz, 36 dB amplifiers. Spacing between the MCP assembly and anode structure is 7mm with a gap bias of 1.2 kV. The MCP and the photocathode are separated by 300 micron-thick Kapton spacers with voltages varied between 100 and 400 Volts. Voltages across the MCP were varied from 1.2 kV to 1.5 kV, with the majority of data taken at three voltages: 1.36, 1.44, and 1.5 kV

2.3.3. Processing of Data and Quality Cuts

In our data analysis chain, we apply a series of basic quality cuts. We require that the central stripline contain one good, primary pulse. We define a primary pulse as one which falls withing a time window based on an estimate of the transit time for the light to reach the MCP after hitting the photodiode and for the signal to propagate to the scope. The size of the window was determined by hand to be small enough to exclude nearly all prepulses and/or afterpulses but large enough keep all primary pulses, even if changes in operational voltage change the arrival time of these pulses by a few hundred picoseconds. Our definition of a "good" pulse is one with a "significance" value above 6, where significance is defined as the peak value of the pulse minus the baseline (determined by averaging the first 100 points of the trace) and divided by an estimate of the noise (determined by calculating the standard deviation of the first 100 points).

There is the concern that our quality cut, requiring pulses with a signal-to-noise of approximately 6, would shape the lower end of our pulse height distributions. We generated a series of toy simulations, taking the average pulse shape from data, scaling it to generate a spectrum, and combining it with randomized noise, chosen to match the noise observed in data. Looking at the RMS of the first 100 points in our oscilloscope data over several runs, we determined this noise value to be 3.2 mV. Using our toy simulations, we generated a flat spectrum of MCP signals in pulse-height, combined with 3.2 mV noise, and applied our selection cuts. We determined the efficiency for selecting these pulses

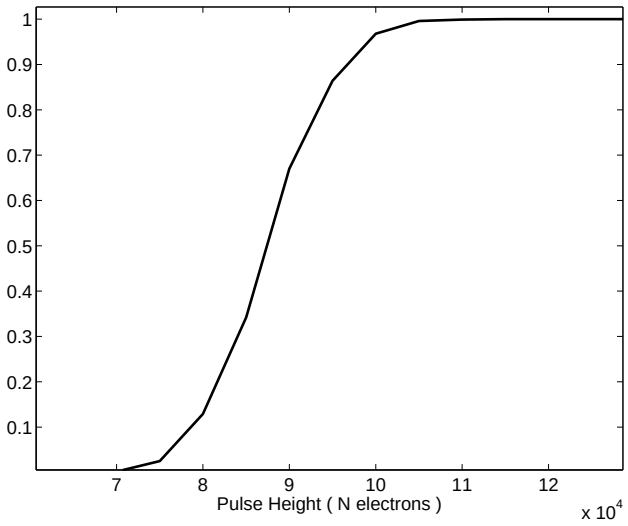

Figure 3: Selection efficiency of our pulse quality cuts as a function of pulse height (number of electrons produced per pulse.

(the ratio of those pulses that pass our cuts to the total number) in bins of pulse height. Figure 3 shows this efficiency function. The selection efficiency for our basic selection cuts seems to be below the low end of the pulses we recorded at most of our operational voltages.

2.3.4. Reconstructed Observables

Once a good pulse has been identified in the appropriate time window, we begin to reconstruct the key observables of interest: the arrival time and the pulse height (which we define as the total charge contained in the pulse). First we subtract the pedistal of the pulse. We define this pedistal as the average of the first 100 points of the trace, well before the onset of the signal or any RF noise associated with the amplification of the laser pulses. This is used to correct for any low frequency variations in the voltage that would offset the integral. Next, we interpolate and resample the pulse. A smooth, spline interpolation is applied between the time samples and a new set of points is selected with a finer step size, every 500 femtoseconds. The new sampling is chosen to be much smaller than the expected resolution of our setup. The interpolation is used in our numeric threshold-crossing algorithm for determining the arrival time and it is used to get as close to the zero crossings of the pulse as possible.

We integrate the pulses numerically, summing each point along the trace multiplied by the time interval between points. Integration bounds are set by the zero-crossing points of the pulse. This integral is divided by the 50 ohm resitance to convert from units of Volt-seconds to Coulombs. In this study we only measure the signal from one set of the stripline anode, the other side is terminated to ground through 50 ohms. We multiply our integral by a factor of two to approximate the total signal. The signal is passed through the combination of a fast amplifier and attenuator. The attenuator was used as extra protection for the high gain, high bandwidth amplifier. Studies were conducted using a 50/50 splitter with the amplifier-attenuator configuration. Currently, we only account for the affect of the amplifier by a constant multiplicative factor on the pulse heights. We integrated unamplified pulsed from an MCP stack and the same pulses through our amplifier-attenuator assembly, and calculated the ratio to be 12.2. Thus, our integrated signal is divided by 12.2. In the future, we hope to use a more sophisticated, shape-based correction for the effects of the amplifier. Finally, we convert from units of Coulombs to number of electrons.

What we call a "pulse height" in this paper refers to the total charge out of the MCP. It is not a gain in the sense that the number of input electrons is not necessarily one. Rather we measure the distribution of charge per pulse out for a fixed incident laser intensity in. The laser intensity can fluctuate from pulse to pulse and over longer time scales. We record average intensity and our trigger signal does record the pulse to pulse variation. However, since we operate the laser at intensities that produce only a few photoelectrons, smooth variations in laser intensity are manifest as quantized variations in the average number of electrons produced. This makes it difficult to compare pulse heights.

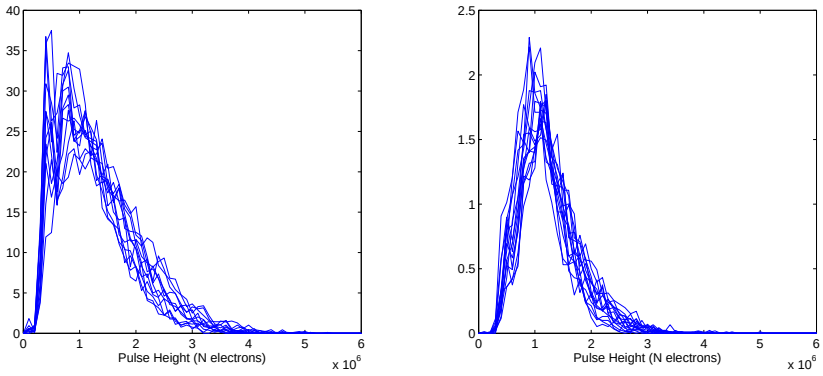

Figure 4: Typical pulse height distributions for (a) 20 nm MgO MCP and (b) 20 nm Al2O3 MCPs at several different positions along the MCP

However, the average pulse height over various runs can be corrected to account for variations in average intenstity.

At the moment we use constant-fraction thresholds to determine the arrival time of each pulse. We average the times of two different threshold crossings 25% and 75% to achieve a more robust result.

2.4. Experimental Results

Figure 4 show some hand selected, typical pulse height distributions (PHDs) for MgO and Al_2O_3, taken at various positions on the MCP in the direction along the transmission line. These PHDs we reconstructed from single plates, where the laser intensity was tuned high enought to produce 6 photoelectrons per pulse. However, we expect that fluctuations in the laser intensity make it difficult to exactly compare these distributions, since a change in the number of PEs would have a quantized effect on the shape.

Regardless, it should be noted that the PHD does not represent the gain of the MCP. Rather, it is the charge produced per pulse for a given laser intensity and set of operational voltages.

One of the challenges involved with interpreting the shape of the pulse height distribution is that actually represents the sum of several pulse height distributions corresponding to different numbers of incident photo electrons. For a given laser intensity we would expect a Poissonian distribution of photoelectrons produced on a hit by hit basis (is this true?). A further complication is that the laser intensity itself can fluctuate by about 20%.

While it is difficult to correct for the quantized features in the shape of the PHD, based on variations in laser intensity, we can correct the average gain for differences in laser intensity. We can measure this average gain for different positions and voltage settings.

Figure 5 shows the transit time disrtibuion of pulses in the lowest gain and highest gain regions of the plate. The transit time spread (TTS) of the reconstructed MCP pulses varies inversely with the gain. This is as we would expect, since the higher the gain, the better the signal-to-noise and the smaller the noise induced fluctuations on the measured arrival time. The curves for both MCPs seem to plateau at just below 50 picoseconds.

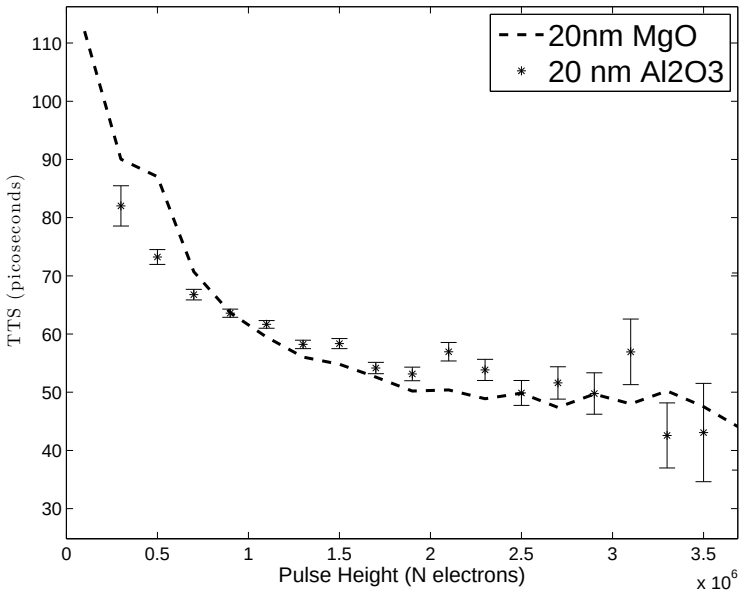

Figure 5: Transit time spread versus pulse height for 20 nm MgO and 20 nm Al2O3

3. The Simulation

3.1. Simulation Overview

A full 3D Monte Carlo Simulation code "MCS" [6, 7, 8] was developed to model microchannel plate (MCP) amplifiers end-to-end. The code can simulate a variety of MCP systems, including single plates, chevron pairs, Z-stacks and several experimental geometries. Many different physical phenomena are taken into account with the numerical models implemented in the code: photo- and secondary emission, variations in the first strike, 3D fringe fields, saturation, end-spoiling phenomenon etc.

The numerical algorithm uses a Monte Carlo method to generate random photo- and secondary electrons, then step these particles through electromagnetic fields, and accumulate the statistical properties of the particle propagation. It can evaluate all needed parameters of MCP amplifiers: gain, pulse shape, arrival time, angular and energy distribution of particle strikes and outgoing particles in pre-defined cross-sections. Each component of the whole device can be simulated seperately, saving the intermediate data in the database, and can be used to various multi-stage designs.

An important element of this model is the inclusion of forward-scattering (FS) in the formation of avalanches. Many early MCP models account only for the production of true secondary electrons when a primary electron strikes the MCP wall. However, there is a non-negligible probability that an incident primary electron will undergo quasi-elastic scattering resulting specular reflection. This process can occur in addition to the production of true secondary electrons, since the energy of the SEY is negligible compared with the incident energy. These so-called back-scattered electrons will accumulate as the avalanche propagates down the pore. Unlike secondary electrons, which are typically low energy and emitted in random directions, FS electrons keep most of their energy and continue to propagate at grazing incidence. They are therefore more likely to produce further secondaries and travel faster down the pore. The forward-scattering process occurs in addition to the production of secondary electrons. Since the energy of the secondary electrons is small compared with the incident primary, the probability of forward-scattering should be relatively independent of the probability of secondary electron production.

Figure 6 shows the coordinate system used in this model.

3.2. Model Inputs

The complete set of initial data includes the photoemission data (geometry shape, angular, energy, spatial and time distributions), MCP properties (geometry of each plate - thickness, pore diameter, bias angle, end-spoiling area,

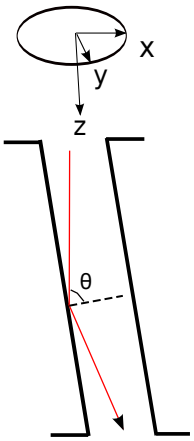

Figure 6: A schematic representing the coordinate system used to describe the geometry of an MCP pore.

gaps; applied voltage) and anode data (geometry, gap, applied voltage), as well as the material properties of secondary emitters for true secondary and forward-scattering electrons. Both the true secondary electron yeild and the forward-scattering probabilities depend on incidence angle and striking energy.

There are different approaches to represent the SEY data. The analytical model by A. Guest [9] is a popular one. Here the SEY σ is represented by a formulae

...

where θ is an incident angle, V - impact energy, V_{max} is an impact energy corresponding to a maximum SE yield of σ_m, α is a surface absorption factor, β is a smoothness factor (β= 0.55 for $V < V_{max}$, and β=0.25 for $V > V_{max}$).

A more complete model should use experimental SEY-curves for any particular secondary emitter material, and the particular thickness of the material. Experimental data typically describes these properties for electrons striking at normal incidence (θ=0) vs. impact energy V. Then we determine the angular dependence through a seperate simulation of the material properties (see Fig **??**), based on semi-analytical models [].

3.3. Theoretical Treatment of Experimental SEY Data

Monte Carlo (MC) simulations, empirical theories, and comparison with experiments were used to identify the influence of various incidence angles and the contribution of back-scattered electrons on the emissive properties of various materials and used to feed this info for calculation of the Gain and Transit Times for microchannel plates (MCPs). The method was applied to Al2O3 and MgO of various thickness and surface quality. The calculated SEE data were fitted to the experimental secondary emission yield (SEY) data obtained by Slade at normal electron impacts. The angular dependences of SEE were obtained by fitting two parameters of the SEY: maximum yield and energy at the maximum value of yield to external angular MC data. The SEY data were calculated at oblique angles of the primary electrons in the interval of 0-80. By using an empirical dependence developed in our previous paper [10]:

$$(\delta/\delta_m) = 1.11(E/E_m)^{-a}[1 - e^{-2.3(E/E_m)^b}] \quad (1)$$

Where the constants: a, b were obtained from Table 1 for Al2O3 and MgO.

Based on eq. (1) and Table **??** a parameterized set of the SEY dependencies was developed where two variables were used: E, the primary electron energy and , the incidence angle for primary electrons, for Al2O3 and MgO.

[PUT TABLE HERE.....]

The angular dependence for Al2O3 was fitted by an expression derived in a previous papers [10].

$$E = 0.025\theta^2 - 0.53\theta + 350.0[eV] \quad (2)$$

$$SEY = 0.0002\theta^2 + 0.006\theta + 3.1[1/electron] \quad (3)$$

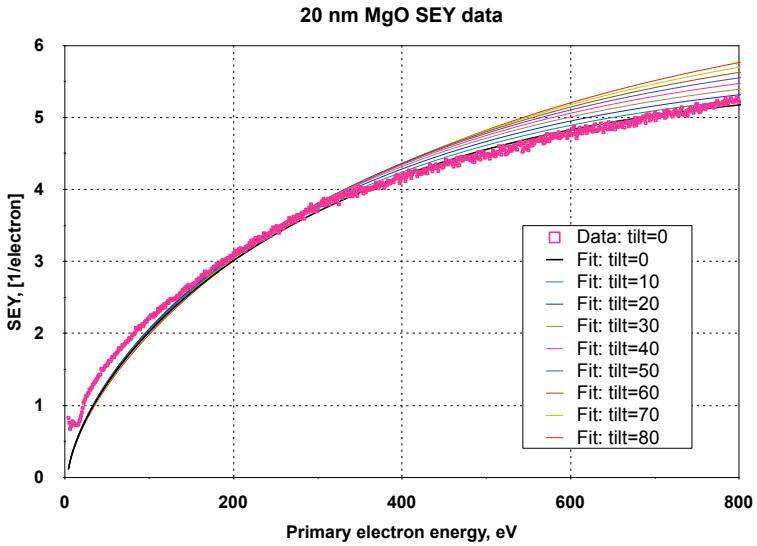

Figure 7: MATERIAL: SEY data, taken at normal incidence for 20 nm MgO sample, overlayed with theoretical fits at various angles of incidence (tilts).

The SEY and the energies at maximum at different angled for MgO were calculated by MC program and fitted to eq. **??**.

Three plots showing the fits for 20nm MgO, 20 nm Al2O3, and 2nm MgO. The energy dependence of forward-scattered electron coefficients (FSCs) for various primary electron incidence angles was calculated by Monte Carlo programs [11, 12, 13] for both materials, and the results were compared with experimental average values obtained in the literature.

Forward-scattering, the quasi-elastic reflection of high energy, primary electrons can make a significant contribution to the gain and timing characteristics of MCPs.

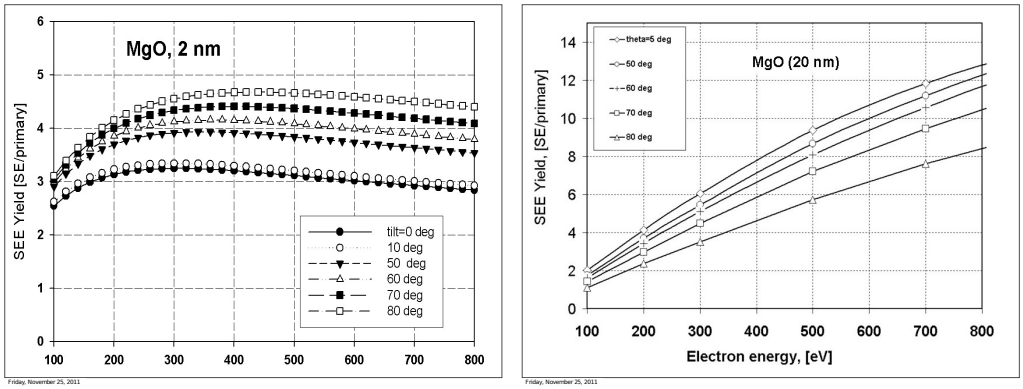

Figure 8: (a) Energy dependence of MgO (2nm) secondary emission yields calculated by a Monte Carlo method for different primary electron incoming angles and different primary (b) Energy dependence of MgO (20nm) secondary emission yields calculated by a Monte Carlo method for different primary electron incoming angles and different primary electron energies.

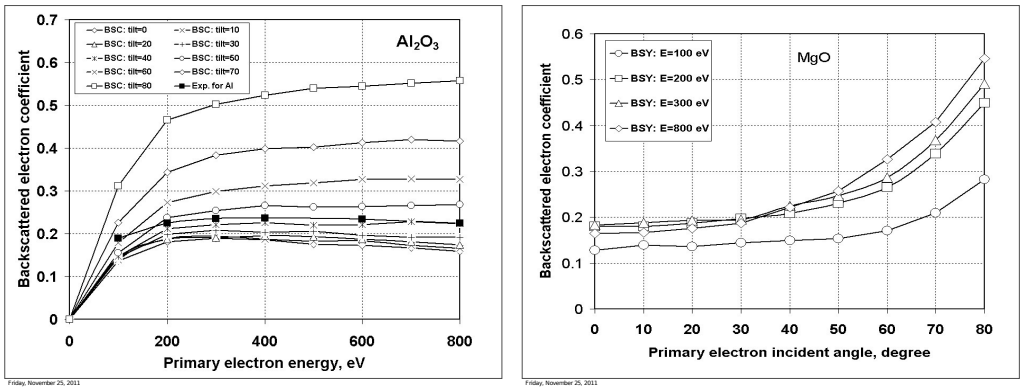

Figure 9: (a) Energy dependence of Al2O3 forward-scattered electron coefficients at different electron incoming angles. Solid symbols are experimental values for pure Al [6]. (b) Energy dependence of MgO forward-scattered electron coefficients at different electron incoming angles.

3.4. Full Avalanche Simulation

Once the material-level properties of the MCP pores are measured and modeled, they can be used as inputs into MCS. MCS individually tracks each electron through the MCP pore, randomly generating outcomes for each collision with the pore wall according to the probabilities given by these inputs.

3.4.1. Electron Propagation Through the Pore

Having the random position, angle, and energy for an ensemble of initial photoelectrons we propagate the particles using a 2^{nd}-order Euler's scheme

$$\vec{r}_i^{\,n+1/2} = \vec{r}_i^{\,n} + \frac{\Delta t}{2}\vec{v}_i^{\,n}, \tag{4}$$

$$\vec{v}_i{}^{+n+1} = \vec{v}_i^{\,n} + \frac{e}{m}\left\{\vec{E}\left(\vec{r}_i^{\,n+1/2}\right) + \frac{1}{c}\left[\vec{v}_i^{\,n} \times \vec{B}\left(\vec{r}_i^{\,n+1/2}\right)\right]\right\}, \tag{5}$$

$$\vec{r}_i^{\,n+1} = \vec{r}_i^{\,n+1/2} + \frac{\Delta t}{2}\vec{v}_i^{\,n}, \tag{6}$$

where $\vec{r}_i^{\,n}$ is a position, and $\vec{v}_i^{\,n}$ is a velocity of i-th particle at the tome moment n; Δt is an integration step; e is a charge, and m is a mass of particle; $\vec{E}$ and $\vec{B}$ are vectors of electric and magnetic field; c is a speed of light.

At each time step, we check if the particle strikes the wall. If so, the incident particle can produce a cascade of secondary particles (strike event), otherwise the incident particle died at the wall.

3.4.2. Production of True Secondary Electrons

In the event of a strike event, we evaluate the number of secondary electrons produced, the current, energy, and the motion direction for each daughter particle. The number of secondary electrons is randomly chosen according to a Poissonian distribution with a mean value correspeonding to the secondary electron yeild curve of the material.

$$f(k,\mu) = \frac{\mu^k}{k!}e^{-\mu}. \tag{7}$$

where f is a probability to generate k particles with mean value μ.

The angular distribution of true secondary particles obeys Lambert's law

$$f_\theta = \frac{\cos\theta}{\pi}, \tag{8}$$

but their energy distribution chosen according to the Chung-Everhardt's law [17]

$$f_V = 6V\frac{\phi^2}{(V+\phi)^4}, \tag{9}$$

where ϕ is a work function of the electron.

Figure 10 shows the energy and angular distributions of out-going secondary electrons.

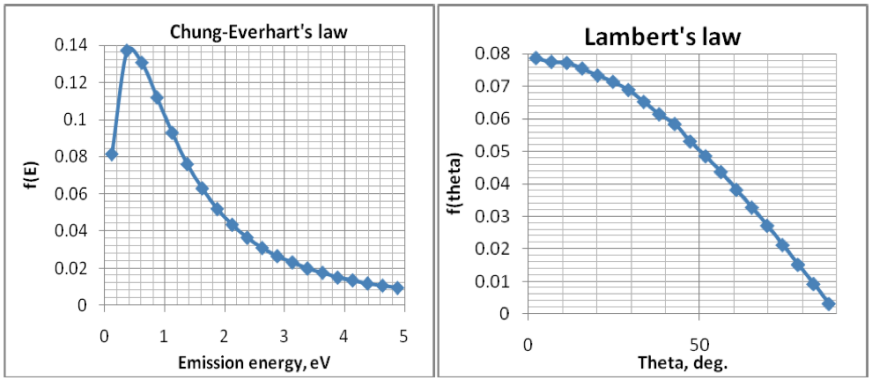

Figure 10: A plot showing the Chung Everhart distribution, describing the outgoing energies of true secondary electrons, and Lambert's Law describing the outgoing angle.

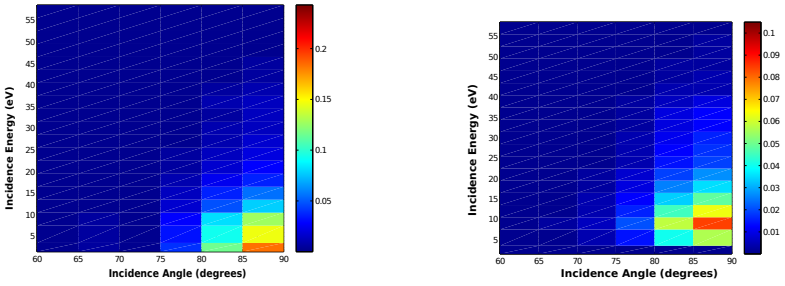

Figure 11: A 2D scatter plot showing the striking energy versus striking angle for (a) all strikes in a cascade and (b) only those strikes that produce further secondaries

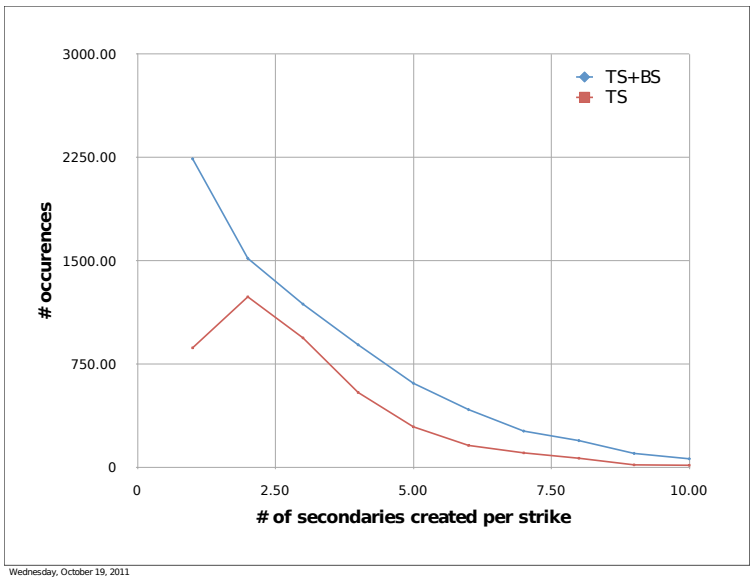

Figure 12: The distribution of the number secondary electrons produced per strike

3.4.3. Specular Reflection of Primary Electrons and Its Impact on Gain and Timing Characteristics

A complete model of secondary emission should include as true secondary particles as back scattering (FS) ones. In MCS, the FS effect is characterized by the probability to create the FS electron, one of k particles of strike event. FS electron undergoes the mirror reflection. It means that its initial energy equals to the energy of incident particle, and its initial angle relatively the normal vector to the surface equals to the angle of incident electron. But the probability is not a constant for a particular material. It is a function of angle and energy V of incident particle, similarly to the Fig.1.

The reflected primaries play an interesting role in the development of avalanches. Perhaps the most interesting feature of forward-scattering lies in the transision from the first and second strikes in the pore. In the absence of FS, one would not expect the gain at a certain MCP voltage to depend on the photocathode voltage. Each strike would be statistically independent. However, the presence of forward-scattering would mean that a fraction of the second strikes in the pore would consist of reflected primary electrons. These forward-scattered primaries retain their prior energy from the first strike, so the average energy of the second strikes would depend on the energy of the first strikes and, therefore, on the accelerating potential from the photocathode to the MCP. The second strike would effectively remember some of the kinematics set by the photocathode voltage.

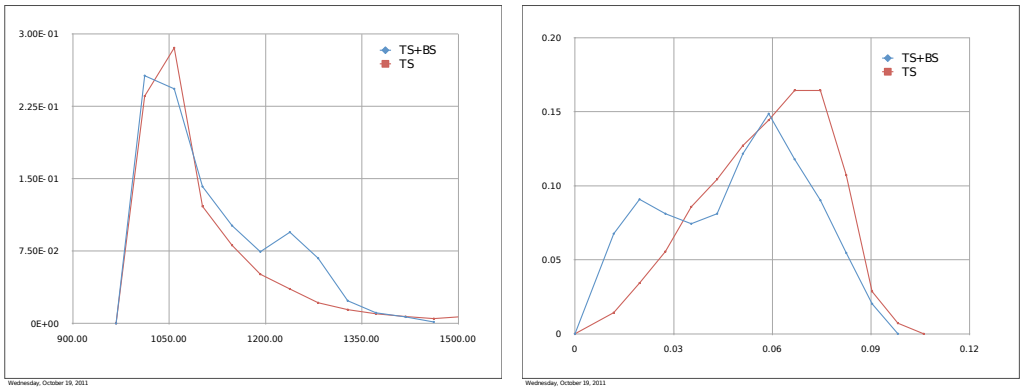

Figure 13: (a) The energy spectrum of electrons exiting the MCP pore (in eV), with and without specular reflection (b) The angular spectrum of electrons exiting the MCP pore (in radians), with and without specular reflection

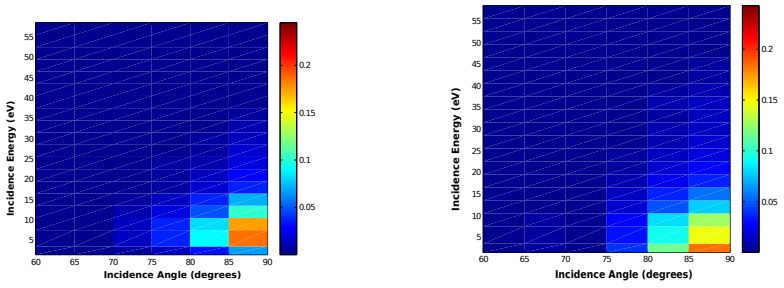

Figure 14: A two dimensional scatter plot showing striking energy versus striking angle for electrons in an MCP with (a) with true secondary production only (no FS) (b) Both true secondary production and forward-scattering.

4. Comparing Simulations-Based Predictions with Experimental Results

We peformed the simulation-data comparison as a partially blind analysis. Our simulation group was given access only to data collected from the MgO coated MCP. After they we satisified with the tuning of their model and produced simulations predicting the gains and arrival time distributions for the Al_2O_3, they were given acess to the corresponding data.

Despite our best efforts to tune the absolute gain in the data a simluations, we were unable to achieve direct agreement, due at least partially to the high sensitivity of predicted gain on the scale in our SEY curve at low energies. Additionally, in order to achieve measurable signals, we required laser intensities operating beyond single photoelectron production and applied voltages on the MCPs above conventional field strengths. The ambiguity in the number of photoelectrons, coupled with the inability to detect low gain pulses made a direct side-by-side comparison of the average measured pulse height with the simulations impossible. For these reasons, we will typically show simulations along side our experimental results, in order to demonstrate trends and qualitative features, without correcting the scales. We will also rely heavily on ratios to cancel this systematic.

Since we do not know the exact number N of photoeclectrons produced per each laser pulse, what we call the "average pulse height" is not the gain but rather N times the gain. However, monitoring our laser, we were able to maintain a consistent average laser intenstiy, so that direct comparisons could be made between our two MCP samples and among data taken at various voltages.

Among the critical relationships that we studied in this paper were the dependences of the average pulse height (charge per laser pulse) on the various operational voltages of our MCP detector system. The voltage across the photocathode (V_{PC}) gap accelerates photoelectrons produced in our aluminum photocathode toward the MCP surface, thereby setting the energy of the first strike in the avalance. Voltage accross the MCP itself (V_{MCP}) sets the accelerating potential for the rest of the avalanche and has a strong, non-linear impact on the MCP gain.

4.1. Insensitivity of Al_2O_3 MCP to Changes in Photocathode Voltage Above 100V

Figure 15 shows the average pulse height versus V_{PC} for the 20 nm MgO MCP operating at 1.5 kV, along that of the 20 nm Al_2O_3 plate. As we would expect from their respective SEY curves, the MCP coated with 20 nm of Al_2O_3 shows much less sensitivity to the first strike-energy than the 20 nm MgO MCP for first strikes above 100 eV. In this range, the SEY for Al_2O_3 begins to plateau, while that of MgO continues to increase (see Fig 1).

4.2. Predictions and Observations of Forward Scattering Effects in MgO

One particularly interesting effect predicted by the simulation provides an experimental handle for observing and potentially quantifying the effects of forward scattering in the MCP. In an MCP avalanche without FS effects, the kinematic properties of an incident primary electron strongly determines the number of secondary electrons produced by a strike, but it has little bearing on the angles and energies of those daughter particles. This is because the low energy and direction of true secondary electrons is largely random, according to Chung-Everhart distribution and Lambert's Law, respectively, regardless of the energy of the incident primary electron. As a consequence, the energy of the $(n+1)$th strike has little dependence on the properties of the nth strike. They can be treated as statistically independent and therefore factorized. Experimentally, there is one striking electron in the avalanche that can be controlled independently from the rest of the cascace, namely the first photoelectron. By controlling the voltage across the gap between the photocathode and MCP, we can control the energy of that strike. Similarly, by setting the operational voltage across the MCP, we can control the gain over the rest of the avalanche. If the energies and angles of the daughter electrons from the first strike are independent of the energy and angle of the first photoelectron, then the gain dependence on V_{PC} should be factorizable from the gain dependence on.

$$G_{TOTAL} = G_1(V_{PC})G_{2..N}(V_{MCP}) \tag{10}$$

Therefore, the ratio of the total gains at two different V_{MCP} settings, should not depend on V_{PC}. If we plot this ratio as a function of V_{MCP} we should see a flat line.

In contrast, the presence of forward scattering will introduce a correlation between the first and second strike. Since forward scattered electrons retain the majority of their original energy, the energy of a second strike will depend on the energy of the first strike. This means that the gain increase for a particular increase in V_{MCP} builds on the

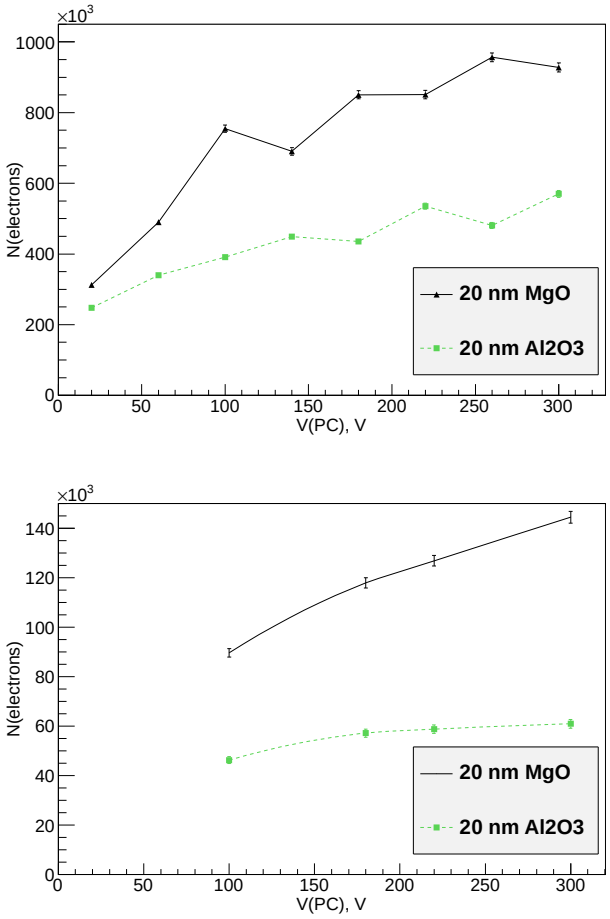

Figure 15: A plot comparing the integrated charge per MCP pulse observed as a function on V_{PC} for an MgO and Al_2O_3 MCP at 1.5 kV in (a) data and (b) simulation.

energy of a scattered electron with energy set by V_{PC}. Put another way, the effect of a change in MCP voltage should amplify different first strike energies differently. We can represent this relationship through:

$$G_{TOTAL} = G_1(V_{PC})G_{2..N}(V_{MCP})\rho(V_{PC}, V_{MCP}) \tag{11}$$

The ratio of gains at different MCP voltages will now depend on the potential across the photocathode gap. If we plot this ratio as a function of V_{MCP} we would see a relationship that is no longer consistent with a flat line. Figure 16 (a) demonstrates this effect, as predicted by our simulations. When forward scattering is absent, the simulation shows a constant multiplicative relationship between the gain at two different MCP voltages, regardless of the voltage across the photocathode gap. With FS turned on, the model shows a roughly 30% varation in the ratio between these two MCP voltages over a range of first strike energies from 100 eV to 260 eV. The forward scattering effect in this model depends on our choice for the overall normalization of the forward scattering probability. This value is not yet strongly constrained, and so the size of the FS effect on the ratio of MCP gains could be larger or smaller depending on the value in actuality. Figure 16 (b) shows this ratio as measured in data. Error bars are statistical only, since we do not have an accurate model of our systematics, which are related to variations in the pulse-by-pulse laser intensity. These data are noisy, but still show a hint of a trend inconsistent with a straight line fit (overlaid in red). A linear fit (shown in blue) gives a slope of around 0.0004 per Volt and much better agreement.

4.3. Insensitivity of Al_2O_3 MCP to Changes in MCP Voltage Above 1.3 kV

Another interesting trend predicted by our simulation was the low sensitivity of the Al_2O_3 MCP to variations in MCP voltage from 1.36 to 1.5 kV. Figure 17 shows the average pulse height as a function of V_{PC} for three different V_{MCP} values (1.36 kV, 1.44 kV, and 1.5 kV) in the MgO and Al_2O_3 MCPs, as observed in data and as predicted by the Monte Carlo simulation. In the data, the average pulse height versus V_{PC} curves are indistinguishable within our statistical uncertainties. Our simulation shows an observable difference between the gains at all three voltages, but a spread much smaller than that of the MgO MCP. This is interesting since the majority of striking energies in the MCP are below 100 eV (see Fig **??**), and in this region the SEY curves of MgO and Al_2O_3 are nearly identical. There are several possible explanations for this. One is that, at such high operational voltages, the change in gain is dominated by the tail of high energy collisions above 100 eV. Another possible explaination is the competing affect of electrons striking at higher energies, producing more secondary electrons, with a decreasing number of average strikes in the pore since the electrons will travel further between strikes at higher voltages. Fortunately, our simulation demonstrates the same effect. Looking at kinematic variables describing avalanche formation in the pore, we can use the simulation to clarify a possible mechanism for the insensitivity to MCP voltage shown in Al_2O_3...(need some plots/help from Valentin on this)...Only, in this case we need the simulations to provide insight into the kinematics of the electrons. If small variations in the MCP voltage from 1.36-1.5 kV tend to enhance the high energy tail of the distribution of striking energies, this would mean more gain in the MgO MCP but not the Al_2O_3.....

4.4. Ratio of gains between MgO and Al_2O_3

Figure 18 shows the ratio of the pulse-height versus V_{PC} curves for MgO divided by Al_2O_3 in both data and simulation. The predictions made by our model show good agreement with the results of our experimental MCP measurements.

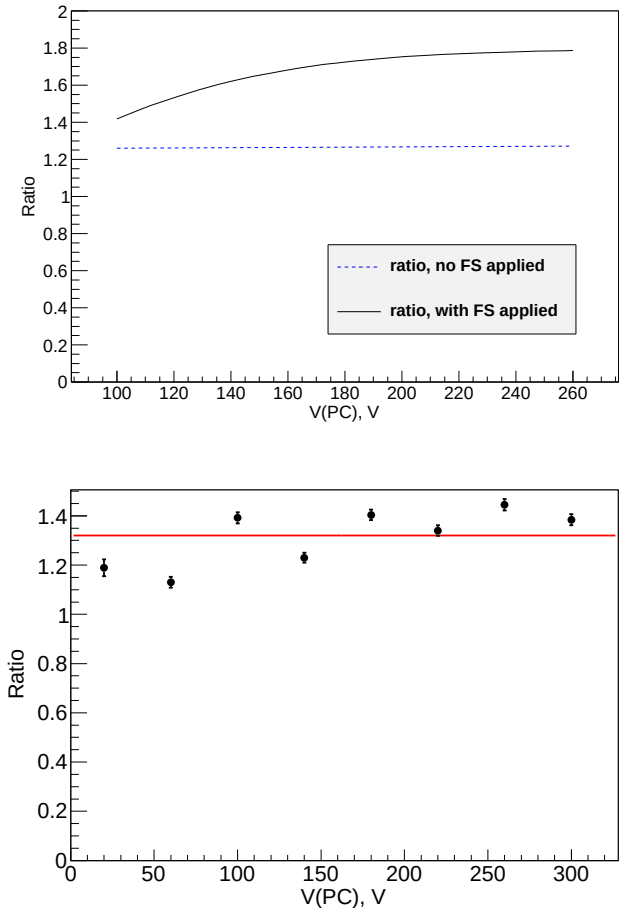

Figure 16: (a)The ratio of simulated gains from a single MgO MCP at $V_{MCP} = 1500V$ divided by the gains at $V_{MCP} = 1360V$ and plotted as a function of V_{PC}, for a model with no forward scattering included (blue dashed line) and a model with forward scattering included (black solid line). In the model with FS electrons, the gain dependence on the first strike energy, set by V_{PC}, can no longer be separated from the gain dependence on V_{MCP}. (b) The ratio of measured average pulse heights from a single MgO MCP at $V_{MCP} = 1500V$ divided by the gains at $V_{MCP} = 1360V$ and plotted as a function of V_{PC}.

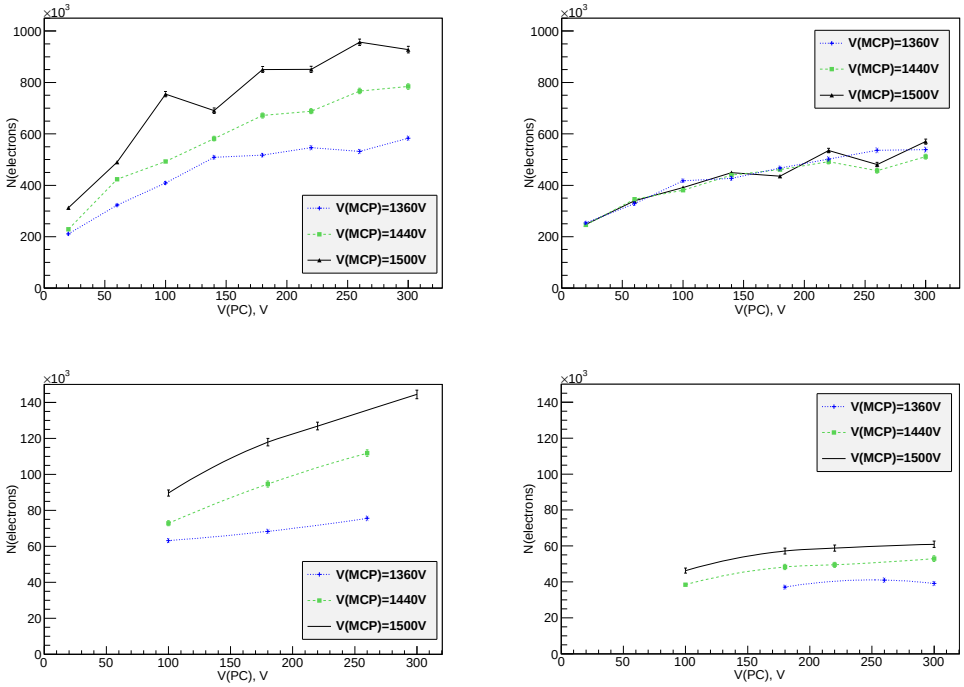

Figure 17: Avg pulse height Vs. PC voltage for 3 different MCP voltages from (a) 20 nm MgO (b) 20 nm Al2O3 samples compared with the simulations for (c) MgO and (d) Al2O3

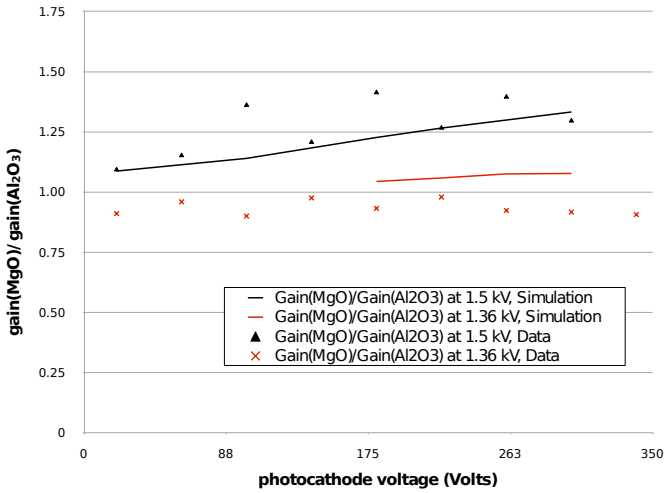

Figure 18: Ratio of the average gain above 800k between 20 nm MgO and 20 nm AL2O3 as a function of PC voltage for two different MCP voltages and for both data and simulations.

5. Conclusion and Future Prospects

In this paper we presented a Monte Carlo model for studying how MCP performance depends on the experimentally measured electron yield and scattering properties of the materials used to make the channel plates. The results of this simulation were compared with experimental measurements of MCPs fabricated using those same materials. Certain experimental challenges prevent us from making a direct quantitative comparison of the average gains for the single-plate data presented in this paper. Nonetheless, the simulation correctly predicted a vareity of interesting qualitative relationships in these data and, direct comparisons made using ratios of gains (where these systematics cancel) gave impressive agreement with the data. The techniques presented in this paper show promising capabilities for helping to understand the relationship between device operations and basic material physics such as electron scattering. Future measurements, improving on these results can give an experimental handle on forward scattering of electrons in microchannel plates and more precise constraints on our models. These models can in turn be used to guide the design of custom, highly optimized MCP detectors.

Acknowledgements

The submitted manuscript has been created by UChicago Argonne, LLC, Operator of Argonne National Laboratory (Argonne). Argonne, a U.S. Department of Energy Office of Science laboratory, is operated under Contract No. DE-AC02-06CH11357. The U.S. Government retains for itself, and others acting on its behalf, a paid-up nonexclusive, irrevocable worldwide license in said article to reproduce, prepare derivative works, distribute copies to the public, and perform publicly and display publicly, by or on behalf of the Government.

[1] S. George, Atomic layer deposition: An overview, Chemical Reviews 110 (2010) 111–131.
[2] N. Sullivan, P. de Rouffignac, D. Beaulieu, A. Tremsin, K. Saadatmand, D. Gorelikov, H. Klotzsch, K. Stenton, S. Bachman, R. Toomey, Novel microchannel plate device fabricated with atomic layer deposition, Proceedings of the Ninth International Conference on Atomic Layer Deposition.
[3] J. W. Elam, S. M. George, Growth of zno/al_2o_3 alloy films using atomic layer deposition techniques, Chemistry of Materials 15 (2003) 1020–1028.
[4] S. Jokela, I. Veryovkin, A. Zinovev, J. Elam, Q. Peng, , A. Mane, The characterization of secondary electron emitters for use in large area photo-detectors, Application of Accelerators in Research and Industry AIP Conf. Proc. 1336 (2011) 208–212.
[5] E. Oberal, et al, in this proceedings.
[6] V.Ivanov, T.J.Roberts, R.Abrams, H.Frisch, Large area photo-detectors with millimeter and picosecond resolution: Simulations, PAC09, 4-8 May , Vancouver, Canada.
[7] Z.Insepov, V.Ivanov, H.Frisch, Comparison of candidate secondary electron emission materials, Nucl. Instrum. Methods B 268 (2010) 3315–3320.
[8] Z. Insepov, V. Ivanov, S. J. J. et al., Comparison of secondary electron emission simulation to experiment, Nucl. Instrum. Methods A ?? (2010) ???–???
[9] A. Guest, A computer model of channel multiplier plate performance, Acta Electron 14 (2011) 79–97.
[10] Z. Insepov, V. Ivanov, S. Jokela, M. Wetstein, Comparison of back-scattering properties of electron emission materials, Proc. of 2011 Part. Accel. Conf. TUP005 (2011) 1–3.
[11] D. Joy, Monte carlo modeling for electron microscopy and microanalysis, Oxford Univ. Press.
[12] D. Joy, A model for calculating secondary and backscattering electron yields, J. Microscopy 147 (1987) 5164.
[13] P. Hovington, D. Drouin, R. Gauvin, Casino: A new monte carlo code in c language for electron beam interaction, Scanning 19 (1997) 1–14.